

X-ray single-crystal diffraction study of pyrope in the temperature range 30–973 K

A. PAVESE, G. ARTIOLI

Dipartimento Scienze della Terra, Sezione Mineralogia, Università degli Studi di Milano, Via Botticelli 23, Milan 20133, Italy

M. PRENCIPE

Dipartimento di Scienze Mineralogiche e Petrologiche, Università degli Studi di Torino, Via Valperga Caluso 37, Torino 10100, Italy

ABSTRACT

X-ray single-crystal diffraction data are presented for synthetic pyrope garnet over the temperature range 30–973 K, which extends the range previously studied. The structure refinements allow a detailed geometrical analysis of the polyhedral distortions over this temperature range, the determination of the thermal expansion for bond distances, and the determination of atomic displacement parameters. The problem of static or dynamic disorder of the Mg site is discussed on the basis of the temperature behavior of the atomic displacement tensors, which show no evidence of static disorder on this site. The high-temperature anharmonic contribution to the thermal vibrations is investigated by the use of Gram-Charlier high-order expansion terms of the displacement parameter tensor.

INTRODUCTION

Garnets are widespread minerals in the Earth's crust and upper mantle, and they play a fundamental role in high-pressure and high-temperature petrogenetic processes. The thermodynamic behavior of their solid solutions, principally along the almandine-pyrope, grossular-pyrope, and grossular-almandine joins, has been extensively studied (e.g., Cressey, 1981; Geiger et al., 1987; Berman, 1990; Koziol and Bohlen, 1992). However, a complete understanding of the structural, thermodynamic, and microscopic properties is still lacking.

The general structural formula of garnet can be written as $X_3Y_2Z_3O_{12}$, where X refers to eightfold-coordinated cations (mostly Mg, Fe, Ca, and Mn in naturally occurring garnets), Y is sixfold-coordinated Al, Fe, and Cr, and Z is essentially ^{14}Si . Most natural garnets occur in complex solid solutions and have the highest allowed space group symmetry ($Ia\bar{3}d$) (Novak and Gibbs, 1971). In end-member pyrope ($\text{Mg}_3\text{Al}_2\text{Si}_3\text{O}_{12}$), which is stable only at high pressure as confirmed by geological occurrences and synthesis conditions, the octahedral site is occupied by Al and the large dodecahedral X site is occupied by Mg. Since Mg is significantly smaller than Fe and Ca, which are the X-site cations in almandine and grossular, respectively, there is a geometrical anomaly in pyrope because Mg would fit better into an octahedrally coordinated site. The large difference between the dodecahedral cavity size and the cation radius of Mg suggests that strong vibrational motion and significant deviations from full harmonic conditions could occur together with static disorder of the cation position and distortion of the Mg-centered polyhedron.

Zemann and Zemann (1961) refined the crystal structure of a synthetic pyrope, and Zemann (1962) proposed

a small amount of static Mg disorder to explain the electron density anisotropy observed in the diffraction data at 293 K; they approximated the cation disorder by a statistical distribution over a general position slightly displaced from the special one. Gibbs and Smith (1965) also refined the structure of a synthetic pyrope at room temperature and pointed out a correlation between an anisotropic vibration of the cation and the distortion of the Mg polyhedron, attributing the effect to the large cavity size. Meagher (1975) carried out an X-ray single-crystal diffraction study on a synthetic pyrope in the temperature range 25–750 °C, but difference Fourier maps calculated around the Mg position failed to detect any static disorder. However, a limited number of independent reflections (<60) were employed in this study. In a more recent X-ray single-crystal diffraction study on synthetic pyrope (Armbruster et al., 1992) two data collections were performed at 100 and 292 K, and large and anisotropic thermal vibrations of Mg along the X-O bond were confirmed. Subsequently Armbruster and Geiger (1993) conducted a single-crystal X-ray experiment at 500 K that focused attention on the study of Mg atom dynamics and of strain effects in synthetic pyrope. A strong dynamic disorder of Mg on the X-site was observed. Powder FTIR spectroscopy between 100 and 310 K was also employed to investigate synthetic pyrope, and the results seem to exclude significant subsite disorder (Geiger et al., 1992). Sawada (1993) refined the crystal structure of a natural, nearly end-member pyrope from room-temperature X-ray single-crystal diffraction data. He applied a Gram-Charlier series expansion up to a fourth-rank thermal tensor to test for anharmonic behavior and analyzed the residual electron density in detail; large thermal vibration and strong anisotropy were observed for Mg compared to the other atoms, but no evidence of anharmonicity was found.

Several studies have pointed out the importance of Mg dynamics on the thermodynamic and calorimetric properties of pyrope and its solid solutions. Haselton and Westrum (1980) measured low-temperature heat capacities of synthetic pyrope up to 350 K and noted the anomalously high value for pyrope, which is believed to be related to vibrations in the unusually large eightfold-coordinated site of Mg. Cressey (1981) studied the excess entropies and enthalpies of mixing for the almandine-grossular and pyrope-grossular joins and observed a slightly more positive excess entropy in the Mg-rich garnets than in the Fe-rich members, suggesting that a subsite disorder might exist in the Mg-rich garnets. Kieffer (1979a, 1979b, 1979c, 1980) applied her approximated thermodynamic model to orthosilicates, and she calculated the specific heat of pyrope at constant volume, obtaining values lower than the ones measured calorimetrically in the temperature range 0–200 K. Hofmeister and Chopelas (1991) used a modified form of Kieffer's method for the calculation of the density of states; they compared the thermodynamic properties of pyrope calculated using spectroscopic data with those derived from the calorimetric measurements of Haselton and Westrum (1980). A calorimetric entropy excess was observed and was attributed to subsite Mg disorder. Their calculations based on positional disorder yielded entropy values larger than the observed ones, suggesting that partial site disorder occurred. Gramaccioli and Pilati (personal communication) recently calculated the atomic displacement parameters for pyrope by lattice dynamics and semiclassical potential theory and noticed that only their values for Mg did not match the experimental data of Armbruster et al. (1992). This observation indicates that the Mg motion might not be fully harmonic and confirms the earlier lattice dynamics results of Winkler et al. (1991).

The available studies clearly show that the question of anharmonic motion for Mg and the presence of static disorder in pyrope are still being debated; hence, a structural study of pyrope over a wide temperature range is needed. This study presents a detailed analysis of the structural crystallography of pyrope in the range 30–1000 K using X-ray single-crystal diffraction experiments performed at 30, 300, 773, and 973 K.

EXPERIMENTAL METHODS AND REFINEMENT PROCEDURES

A synthetic pyrope single crystal used in previous X-ray work (Armbruster et al., 1992) was provided by Thomas Armbruster. The crystal had been hydrothermally synthesized in a piston-cylinder device at high pressure and high temperature by Charles Geiger and was subsequently rounded to a sphere of 0.45 mm diameter. The spherical shape enabled a full analytical absorption correction to be applied to the observed diffraction data.

Four sets of intensity data were collected at 30, 300, 773, and 973 K, hereafter referred to as A, B, C, and D, respectively. MoK α X-ray radiation and a graphite monochromator were used. Particular care was taken in the choice of the scan angle width in order to avoid se-

rious peak truncation effects, although the single crystal that was used showed negligible mosaic spread broadening. The data collection at the lowest temperature was performed on a SYNTEX-NICOLET diffractometer equipped with a liquid-He cryostat and a temperature controller. The data were collected by R. Destro following his standard procedure (Destro, 1988). The data were collected using two different crystal orientations so as to identify multiple scattering effects. The stronger reflections were also remeasured with an incident X-ray beam of low intensity to avoid counter saturation effects. All collected data were refined simultaneously with separate scale factors. An ω - 2θ scan mode was employed with a constant scan speed of 1.5 °/min. The room-temperature data (B) were collected on a KM4 K-geometry KUMA diffractometer; an ω - 2θ scan with different velocities according to reflection intensity was adopted, ranging between 0.6 and 0.9 °/min. The C and D high-temperature data were collected on a Siemens P4 instrument in Eulerian geometry. The high temperature was achieved through a continuous N₂ flux, heated by an electric resistance furnace; a Pt-Rh thermocouple placed at the tip of the hot beam driver tube, and previously calibrated using the thermal expansion of a NaCl standard crystal, allowed continuous monitoring of the temperature; temperature stability is considered to be better than ± 10 K. The N₂ flux directly heated the crystal, which was not enclosed in any apparatus. An ω - 2θ scan mode was employed, and velocity was changed according to the intensities of the measured reflections. Details of each experiment are listed in Table 1.

As already discussed by Armbruster et al. (1992), a strong multiple scattering effect is present in pyrope, and it can severely affect the observed intensities to the extent of generating symmetry-forbidden reflections. The $1a3d$ symmetry was assumed because all previous work showed that all apparent extinction violations can be accounted for by multiple scattering effects. The maximum number of possible equivalent reflections was collected (about six for each independent reflection) within the limits imposed by experimental apparatus. During the merging process, all reflections differing from the average by >2.5 esd were considered to have been affected by multiple scattering or extinction and were discarded. For a few reflections, the correctness of this assumption was checked with the simulation program of Rossmann et al. (1990), and it was clearly evident in the observed ψ scans. The data were collected to 2θ angles as high as possible to allow enough flexibility in the $(\sin \theta)/\lambda$ cut-off imposed during the structure analysis, as discussed below. In all refinements, reflections with $I_{\text{obs}} < 3\sigma$ were neglected; experimental weights ($1/\sigma^2$) were adopted; thus more complex and arbitrary weighting schemes were avoided.

Electron density distortion effects on the displacement parameters were avoided by eliminating reflections with $(\sin \theta)/\lambda < 0.5$. This cut-off limit was carefully chosen to utilize a number of reflections large enough to avoid under-determination problems and, at the same time, to limit correlation between the refined parameters and scal-

TABLE 1. Experimental parameters for single-crystal X-ray data collection at different temperatures

T	30 K	300 K	773 K	973 K
Crystal dia. (mm)	0.45	0.45	0.45	0.45
Cell parameter (Å)	11.439(2)	11.4544(2)	11.5129(5)	11.5348(5)
Scan mode	ω -2 θ	ω -2 θ	ω -2 θ	ω -2 θ
Scan angle (°)	3.0 + Δ 12	2.4 + 0.35 \times tan θ	2.4 + Δ 12	2.4 + Δ 12
Upper and lower motor speed (°/min)	1.5–1.5	0.9–0.6	15–1	15–1
2 θ upper limit (°)	109	120	104	104
Meas. refl.	8228	6045	3909	4006
Selected and merged refl.	2254	923	742	654
(sin θ)/ λ cutoff	0.5	0.5	0.5	0.5
Limit $F_{\text{obs}}/\sigma_{F_{\text{obs}}}$	3	3	3	3
Refl. used for refinement	1710	790	461	418
Cutoff range $F_{\text{obs}}/F_{\text{calc}}$	0.7–1.4	0.7–1.4	0.7–1.4	0.7–1.4
Refl. selected in refinement	1458	762	458	408
Ext. coeff., type II	1698(60)	—	908(200)	978(300)
R (%)	1.224	1.368	1.466	1.662
R_w (%)	0.786	1.234	1.360	1.376
χ^2	2.771	2.010	1.742	2.350

Note: the Δ 12 is the $K\alpha_1$ - $K\alpha_2$ angular split.

ing errors. The results of the structure refinements using all reflections show an increase in the atomic displacement parameters of about 5%, as is expected from charge distribution effects, whereas the fractional coordinates of the O atom did not show any significant shift. The extinction correction played a delicate role in the refinement because this parameter correlates closely with the scale factor and the atomic displacement parameters. Several correction models for the treatment of the secondary extinction effects were attempted, and the isotropic correction for a type II crystal (Becker and Coppens, 1974) with a Lorentzian mosaic spread distribution was found to yield the best results. The refined correction factors turned out to be very small, which was expected on the basis of the narrow mosaic spread distribution in the crystal; no correction was necessary for the room-temperature data. No correlation was found between the refined extinction correction factors and the data collection temperature. Reflections that, during the refinement, turned out to have intensities affected by extinction of more than 60% were discarded. No extinction correction was applied or refined for room-temperature data because of difficulties in refinement convergence.

The γ and δ atomic displacement tensors, following the Gram-Charlier expansion and corresponding to third and fourth rank, respectively, were employed to investigate the anharmonic dynamical behavior of the Mg cation. The Gram-Charlier model was chosen following the observations of Kuhs (1988). The higher order tensor coefficients were refined by keeping the optimized second-rank components fixed, because of strong correlations affecting any attempt at simultaneous refinement. No serious correlation between high-order displacement parameters and the extinction coefficient was found. Table 2 reports the results of the final structure refinements.

RESULTS AND DISCUSSION

Structure-temperature relationship

Comparison of the present structure results with the previous work at 100 and 293 K (Armbruster et al., 1992),

at 500 K (Armbruster and Geiger, 1993), and at higher temperatures (Meagher, 1975), shows good general agreement. The largest discrepancies are found in the high-temperature data, probably because of the larger experimental errors and the limited data set utilized by Meagher.

The thermal structural behavior of pyrope is essentially determined by the polyhedral response to temperature. Because of symmetry constraints, the only geometrical variables in the structure are the atomic coordinates of O, which lies on a general position and is related to all deformations of the cation coordination polyhedra. The

TABLE 2. Refined coordinates, second- and third-rank thermal tensor components from data obtained at 30, 300, 773, and 973 K

T	30 K	300 K	773 K	973 K
Al(0,0,0)($\beta_{11} = \beta_{22} = \beta_{33}; \beta_{12} = \beta_{13} = \beta_{23}$)				
β_{11}	0.283(2)	0.520(3)	1.216(7)	1.532(8)
β_{12}	-0.003(2)	-0.002(3)	0.003(5)	-0.006(7)
Si($1/2, 0, 1/4$)($\beta_{22} = \beta_{33}; \beta_{12} = \beta_{13} = \beta_{23} = 0$)				
β_{11}	0.226(3)	0.410(5)	0.921(9)	1.158(9)
β_{22}	0.260(2)	0.479(4)	1.105(8)	1.369(8)
Mg(0, $1/4, 1/6$)($\beta_{11} = \beta_{22}; \beta_{13} = \beta_{23} = 0$)				
β_{11}	0.631(3)	1.622(7)	3.87(2)	4.79(2)
β_{33}	0.393(5)	0.738(8)	1.72(2)	2.13(2)
β_{12}	0.113(4)	0.483(8)	1.06(2)	1.33(3)
β_{11}	0.744(5)	2.11(1)	4.93(3)	6.12(4)
β_{22}	0.518(5)	1.14(1)	2.81(3)	3.46(4)
γ_{113}	-0.004(2)	-0.007(3)	-0.034(8)	-0.06(1)
O				
x	0.032907(8)	0.03295(1)	0.03306(2)	0.03304(3)
y	0.050688(8)	0.05032(1)	0.04963(2)	0.04942(3)
z	0.653311(8)	0.65334(1)	0.65344(2)	0.65354(2)
β_{11}	0.438(4)	0.757(6)	1.72(1)	2.15(1)
β_{22}	0.534(3)	0.939(6)	2.17(1)	2.67(2)
β_{33}	0.359(3)	0.589(5)	1.31(1)	1.64(1)
β_{12}	0.055(3)	0.133(4)	0.314(9)	0.37(1)
β_{13}	-0.096(3)	-0.174(4)	-0.437(9)	-0.55(1)
β_{23}	0.007(3)	-0.029(4)	-0.077(9)	-0.07(1)

Note: β'_i is the i th component of the diagonalized tensor ($\beta, \beta' \times 10^3; \gamma \times 10^4$).

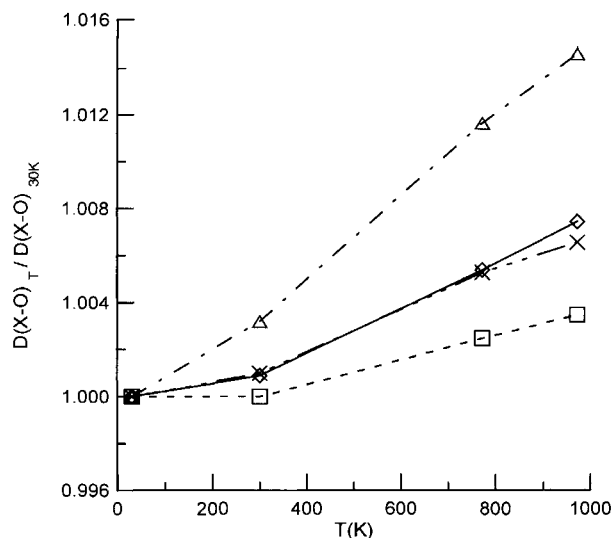


Fig. 1. Ratio of bond length between cation X and O, calculated at temperature T with the value at 30 K. Squares refer to Si-O, diamonds to Al-O, triangles to Mg-O4, and Xs to Mg-O2 bond ratio (see Table 3).

thermal expansion coefficient of any geometrical observable (l) is defined as

$$\alpha(T) = \frac{1}{l(T)} \cdot \frac{dl(T)}{dT} \quad (1)$$

where $l(T)$ is a function of temperature. In the case of pyrope, parabolic functions were employed to fit the observed thermal behavior of all calculated bond distances in the calculation of α according to Equation 1. As shown in Figure 1, all bond distances have the same temperature dependence, showing a rather small change in the low-temperature range (below 293 K) and a steeper slope at higher temperatures. To better compare these results with Meagher's (1975), we also introduce the mean coefficient $\langle \alpha \rangle$, defined as

$$\langle \alpha \rangle = \frac{\Delta(973) + \Delta(773)}{2} \quad (2)$$

where $\Delta(T)$ is

$$\Delta = \frac{1}{l(298)} \cdot \frac{l(T) - l(298)}{T - 298} \quad (3)$$

Thermal behavior of polyhedra

The Si-O bond length variation (Tables 3 and 4) is negligible in the low-temperature range, which is in agreement with the data of Armbruster et al. (1992), whereas in the high-temperature region a small but significant elongation is observed. The values of $\alpha(293)$ and $\langle \alpha \rangle$ are $1.8 \times 10^{-6} \text{ K}^{-1}$ and $5.1 \times 10^{-6} \text{ K}^{-1}$, respectively; the latter is significantly larger than the value of $1 \times 10^{-6} \text{ K}^{-1}$ observed by Meagher (1975). In the Si tetrahedra,

TABLE 3. Distances (Å) and angles (°) calculated from data of Table 2

Bond	30 K	300 K	773 K	973 K
Si-O × 4	1.6338(1)	1.6339(1)	1.6379(3)	1.6395(3)
Si-O* × 4	1.6341(1)	1.6344(1)	1.6391(3)	1.6410(3)
O1-O2 _s × 2	2.4976(1)	2.4964(1)	2.4998(3)	2.5003(4)
O1-O3 _s × 2	2.7492(1)	2.7500(1)	2.7579(4)	2.7616(4)
O1-Si-O2	99.70(1)	99.63(1)	99.48(1)	99.37(2)
O1-Si-O3	114.57(1)	114.61(1)	114.69(1)	114.74(2)
ϕ	27.665(2)	27.500(3)	27.204(6)	27.127(7)
V (Å ³)	2.1905	2.1904	2.2046	2.2105
Q.E.	1.014	1.015	1.015	1.016
A.V.	58.93	59.90	61.73	63.04
Al-O × 6	1.8851(1)	1.8868(1)	1.8953(3)	1.8992(3)
O1-O4 _s × 6	2.6134(1)	2.6184(1)	2.6354(3)	2.6418(4)
O5-O4 _s × 6	2.7173(1)	2.7173(1)	2.7246(3)	2.7292(4)
O1-Al-O4	87.77(1)	87.88(1)	88.09(1)	88.14(1)
O4-Al-O5	92.23(1)	92.12(1)	91.91(1)	91.86(1)
V (Å ³)	8.9115	8.9368	9.0638	9.1193
Q.E.	1.00	1.00	1.00	1.00
A.V.	5.43	4.92	3.97	3.79
Mg-O2 × 4	2.1959(1)	2.1981(1)	2.2076(3)	2.2105(3)
Mg-O4 × 4	2.3334(1)	2.3408(1)	2.3608(3)	2.3678(3)
O4-O7 × 2	2.7688(1)	2.7777(1)	2.8017(4)	2.8112(4)
O4-O6 × 2	2.6992(1)	2.7083(1)	2.7322(3)	2.7391(4)
V (Å ³)	19.9598	20.0999	20.5242	20.6688
Q.E.	0.930	0.930	0.929	0.927

Note: s and u indicate shared and unshared bonds, respectively; angle ϕ is defined in the text; V is the volume of the polyhedron centered on the corresponding cation; Q.E. and A.V. are quadratic elongation and angular variance from Robinson et al. (1971).

* Corrected for thermal motion according to Downs et al. (1992).

the unshared O-O edges are considerably larger than those shared with the dodecahedra, as predicted by Pauling's rules, and they expand at higher rates than the latter (see Table 4), thereby increasing the tetrahedral distortion at high temperature. The tetrahedral volume behaves rather rigidly with observed changes being around 1%. This is in agreement with other silicates (Hazen and Finger, 1982).

The rotation of the tetrahedron around the fourfold axis with temperature can be described by means of the smaller of two angles (ϕ) formed between a given edge of the tetrahedron and the cell vector, where both are perpendicular to the $\bar{4}$ axis (Born and Zemann, 1964). As pointed out by Meagher (1975) and Armbruster et al. (1992), the rotation is linked to an increase in the size of the dodecahedral site, with the Mg-O4 bond having a larger expansion than the Mg-O2 bond. This is clearly evident in Figure 2 where the volume of the dodecahedron (V), the bond-length ratio Mg-O4/Mg-O2, and the angle ϕ are normalized to their values at 30 K and plotted vs. temperature. The roughly linear relationship between ϕ and temperature allows the direct correlation between the ratio Mg-O4/Mg-O2 and the angle ϕ (or between V and ϕ).

The dodecahedral volume and distortion are the most sensitive to temperature variations because the dodecahedron involves the weakest bonds in the structure and shows strong anisotropic expansion. The thermal expansion of the Mg-O4 bond is about twice that of the Mg-O2 bond at all temperatures (Table 4). The latter is sim-

TABLE 4. Bond thermal expansion coefficients computed according to Equation 1; $\langle\alpha\rangle$ defined by Equation 2

Bond	30 K	298 K	773 K	973 K	$\langle\alpha\rangle$
(Si-O)	-1.0(6)	1.8(7)	7(1)	9(1)	5.1(4)
(Si-O)*	-0.7(6)	2.4(7)	8(1)	10(1)	6.0(3)
(Al-O)	1.7(5)	5.4(7)	12(1)	14(1)	9.6(3)
(Mg-O2)	2.7(9)	5(1)	10(2)	12(2)	8.7(3)
(Mg-O4)	11(1)	14(1)	19(2)	21(2)	17.5(3)
(O1-O2) _{sSi}	-2.8(7)	-0.3(8)	4(1)	6(2)	2.6(3)
(O1-O3) _{uSi}	-0.3(3)	2.6(4)	8.0(7)	10.2(9)	6.1(3)
(O1-O4) _{sAl}	5.5(8)	9(1)	16(2)	18(2)	13.5(3)
(O4-O5) _{uAl}	-1.8(2)	1.9(3)	8.6(5)	11.4(6)	6.1(2)
(O4-O7) _{uMg}	10.4(6)	13.8(7)	20(1)	22(1)	18.0(3)
(O4-O6) _{uMg}	12(1)	14(1)	19(3)	21(3)	17.7(4)

Note: s and u indicate shared and unshared and refer to the bond belonging to the polyhedron centered on the cation identified in the subscript. The α coefficient is multiplied by 10^6 .

* Corrected for thermal motion according to Downs et al. (1992).

ilar to the thermal expansion coefficients of the Al-O bond distances. The mean thermal expansion of the Mg-O bond ($13 \times 10^{-6} \text{ K}^{-1}$) observed by Meagher (1975) closely matches our $\langle\alpha\rangle$ value (averaged over Mg-O2 and Mg-O4) of $13.1 \times 10^{-6} \text{ K}^{-1}$. The maximum volume change of the dodecahedron is about 3.5% with respect to the volume at 30 K, which corresponds to the largest polyhedral volume expansion in the structure.

The Al octahedron is the most regular polyhedron; the Al-O bond distance has a significant expansion over the whole temperature range, and its $\langle\alpha\rangle$ value ($9.6 \times 10^{-6} \text{ K}^{-1}$) agrees well with the values reported for ^{101}Al ($8 \times 10^{-6} \text{ K}^{-1}$, Meagher, 1975; $9 \times 10^{-6} \text{ K}^{-1}$, Hazen and Finger, 1982). Unshared edges are longer than shared ones and they have a smaller thermal expansion, leading to a more regular octahedron at high temperature. This is the opposite of the temperature behavior of the tetrahedron, where distortion increases with temperature. Both effects can be described by the angular variance parameters reported in Table 3. The volume expansion of the octahedron is $<2\%$, which is comparable to that observed for the dodecahedron.

Analysis of the atomic displacement parameters

An analysis of the atomic displacement parameters was carried out by referring to the refined coefficients of the β , γ , and δ tensors. The lattice dynamics formalism establishes a general formula to express the displacement parameter tensor β on the basis of eigenvectors and eigenvalues of the dynamical matrix (Pilati et al., 1993a)

$$\beta(p)_{ij} \propto (Nm_p)^{-1} \sum_{\psi\vec{q}} E_{\psi\vec{q}} (2\pi\nu_{\psi\vec{q}})^{-2} e_{p,\psi\vec{q}} \cdot e_{p,\psi\vec{q}}^{*T} \quad (4)$$

where N is the number of unit cells in the crystal, m_p is the mass of the p atom, $\nu_{\psi\vec{q}}$ is the frequency value, $E_{\psi\vec{q}}$ is the average energy of each normal vibrational mode ($\psi\vec{q}$), $e_{p,\psi\vec{q}}$ is the component resulting from the p atom of the eigenvector of the corresponding mode, and e^{*T} is the conjugate of the transpose of vector e . Such atomic displacement parameters are due to the thermal contribu-

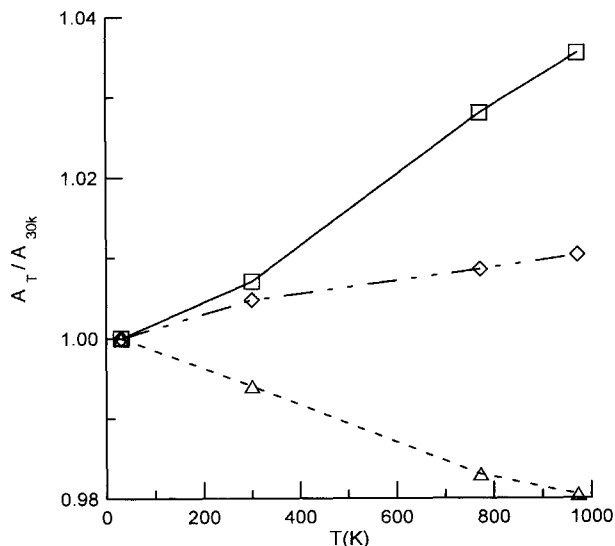


Fig. 2. Ratio of a generic geometric quantity A at temperature T with its value at 30 K. Triangles refer to the angle of tetrahedral rotation ϕ , diamonds to the bond-length ratio (Mg-O4)/(Mg-O2), and squares to dodecahedral volume.

tion alone, and all static disorder effects are neglected. The high-temperature asymptotic behavior of the above expression yields

$$\beta_{ij} \propto T. \quad (5)$$

According to Expression 5, an extrapolation to 0 K of the linear fitting to the experimental high-temperature displacement parameters can, in principle, be used to assess whether static disorder is present because the displacement parameter is predicted to be zero for purely harmonic dynamic behavior. However, the extrapolation of experimental data is not a trivial task because (1) many data points in the high-temperature range are necessary to provide reliable fitting, (2) the atomic displacement parameters should be unaffected by correlations with other parameters in the structure refinement (such as scale factors and extinction coefficients), and (3) Equation 4 is based on purely harmonic effects and neglects all anharmonic contributions that might be significant at high temperatures. Given all the possible biases in the experimental data, a quantitative estimate of any static disorder effect that is based on a linear extrapolation is indeed impossible with a limited data set. However, such an extrapolation might indicate whether the effect is clearly present, especially when supported by the results of theoretical models (Pilati et al., 1993a, 1993b; Gramaccioli and Pilati, personal communication).

Thermal motion of Al, Si, and O atoms. Figure 3 shows the thermal dependence of the diagonal components of the thermal tensor of Al, Si, and O atoms. The 100 K data of Armbruster et al. (1992) and the 500 K data of Armbruster and Geiger (1993) have been added to ours.

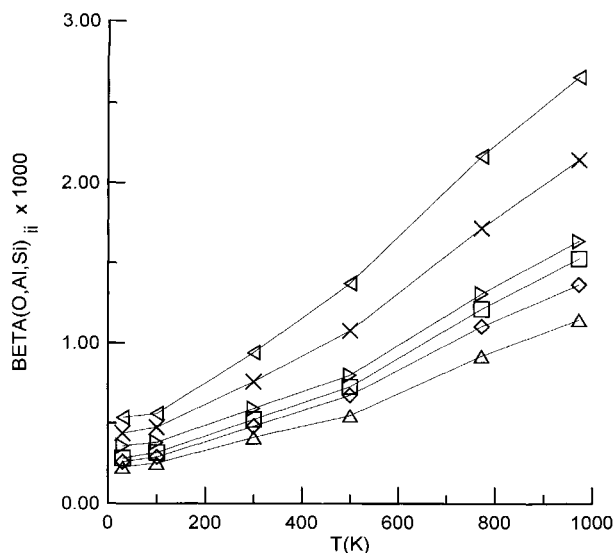


Fig. 3. Diagonal components of displacement tensor β for O, Al, and Si. Results at 100 K of Armbruster et al. (1992) and at 500 K of Armbruster and Geiger (1993) are reported. Squares refer to β_{11} of Al, triangles and diamonds to β_{11} and β_{22} of Si, Xs and right rotated and left rotated triangles to β_{11} , β_{22} , and β_{33} of O, respectively.

The temperature dependence is linear with a steep slope in the high-temperature range, and it flattens below room temperature. This is a clear indication of the effect of the zero-point energy contribution. The overall shape of the curve is predicted from Equation 4. As a first approximation, the displacement parameters obtained from the 30 K data can be considered reliable indicators of the values at 0 K, because of the flatness of the curve in the low-temperature region. Such an approximation is supported by the data at 100 K from Armbruster et al. (1992). The contribution of zero-point motion to the room-temperature displacement parameters is estimated to be in the range 40–60%. These estimates are in agreement with previous experimental low-temperature studies on silicates, such as albite (Smith et al., 1986) and natrolite (Artioli et al., 1984), and with lattice dynamics calculations performed on model structures corundum and bromlite (Pilati et al., 1993a), chrysoberyl (Pilati et al., 1993b), and pyrope (Gramaccioli and Pilati, personal communication) using potentials developed for forsterite, quartz, and corundum. The O atom shows the greatest effects of anisotropic motion, disregarding the Mg atom, which will be discussed below. In particular, the anisotropy of the O atom is reflected in the large β_{33} and β_{22} components. The anisotropy increases in the high-temperature region, as shown in Figure 3 and Table 2.

Thermal motion of Mg. An analysis of the thermal motion of the Mg cation can be best performed by choosing a reference system relative to the diagonalization of the thermal tensor. The new reference axes (\mathbf{a}' , \mathbf{b}' , \mathbf{c}') are defined so that \mathbf{c}' is parallel to \mathbf{c} , and \mathbf{a}' and \mathbf{b}' are along

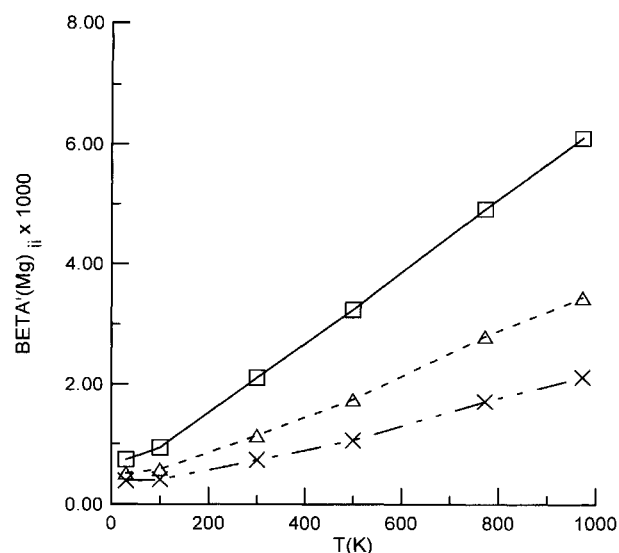


Fig. 4. Components of diagonalized displacement tensor of Mg. Results at 100 K of Armbruster et al. (1992) and at 500 K of Armbruster and Geiger (1993) are reported. Squares represent β'_{11} , triangles β'_{22} , and Xs β'_{33} .

the $[110]$ and $[1\bar{1}0]$ directions, respectively. This transformation corresponds to a rotation of 45° around the \mathbf{c} axis. The new displacement parameters are $\beta'_{11} = \beta_{11} + \beta_{12}$, $\beta'_{22} = \beta_{11} - \beta_{12}$, and $\beta'_{33} = \beta_{33}$.

The thermal expansion of the components of the Mg displacement tensor is directly related to the low-temperature anisotropy, that is, the longer component has the larger thermal expansion coefficient. The anisotropy of the Mg motion is particularly evident along the \mathbf{a}' and \mathbf{c}' axes, and it increases with increasing temperature (Fig. 4). The $\langle u_i u_j \rangle$ tensor, where u_i is the component i of the $\bar{\mathbf{u}}$ vector representing the mean displacement of an atom from its mean position, is related to the refined tensor β by the standard equation (e.g., Giacovazzo, 1992). The motion of the Mg atom is mainly in the (001) plane; in this plane the largest component is parallel to $[110]$ and the smallest to $[1\bar{1}0]$. Linear extrapolations of the high-temperature thermal parameters to 0 K yield the following: $\beta'_{11} = 0.3(3) \times 10^{-3}$, $\beta'_{22} = 0.3(3) \times 10^{-3}$, and $\beta'_{33} = 0.1(1) \times 10^{-3}$. Taking into account that (1) the extrapolated values are within one standard deviation of zero and hence there is a large error affecting the extrapolation, and (2) the largest part of the 30 K thermal parameters is due to the zero-point contribution and matches theoretical calculations (Gramaccioli and Pilati, personal communication), we conclude that there is no evidence of static disorder in the dodecahedral site.

Anharmonic behavior was tested by examining third- and fourth-rank thermal tensors according to the Gram-Charlier expansion discussed above. Table 2 reports the refined components of the γ tensor, which are significantly different from zero. The fourth-rank tensor was refined together with the third-rank one, but it did not

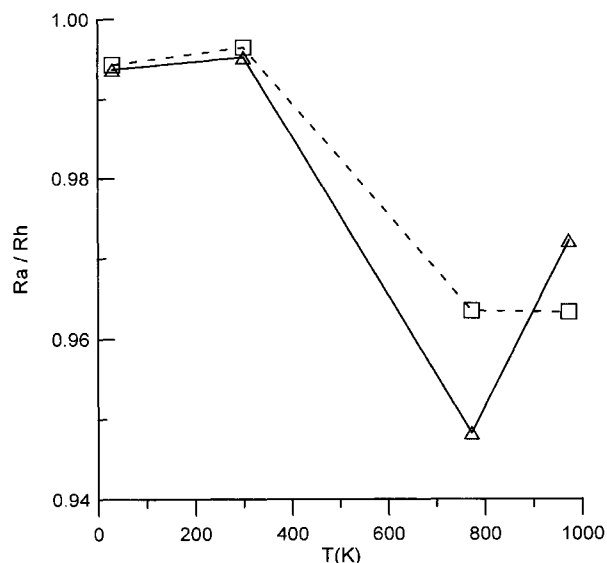


Fig. 5. Ratio of figures of merit for refinements performed with (Ra) and without (Rh) anharmonic thermal tensors γ and δ . Squares refer to R and triangles to R_w .

show any significant contribution to the fit. It is evident that there is a weak but significant contribution of the γ_{113} component, and that there is a constant increase of its magnitude with temperature. It should be noted that the use of the high-order tensor is quite necessary for a good fit to the data at 773 and 973 K, whereas its contribution is negligible at 30 and 298 K. Therefore, no anharmonic behavior can be ascribed to the Mg cation at low temperature, although there are clear indications of nonharmonic vibrations at high temperature, as can be expected from geometrical considerations. Figure 5 illustrates the anharmonic contribution to the lowering of the refinement agreement factors at high temperature.

ACKNOWLEDGMENTS

Financial support was provided by Italian MURST and CNR. R. Destro kindly supplied us with the 30 K data. The authors are grateful to C.M. Gramaccioli and T. Pilati for providing the results of their calculations prior to publication, to T. Armbruster and C. Geiger for providing the pyrope crystal and for useful critical review, and to R.T. Downs for improvement of the manuscript.

REFERENCES CITED

Armbruster, T., and Geiger, C.A. (1993) Andradite crystal chemistry, dynamic X-site disorder and structural strain in silicate garnets. *European Journal of Mineralogy*, 5, 59–71.

Armbruster, T., Geiger, C.A., and Lager, G.A. (1992) Single-crystal X-ray structure study of synthetic pyrope almandine garnets at 100 and 293 K. *American Mineralogist*, 77, 512–521.

Artioli, G., Smith, J.V., and Kvik, Å. (1984) Neutron diffraction study of natrolite, $\text{Na}_2\text{Al}_2\text{Si}_3\text{O}_{10} \cdot 2\text{H}_2\text{O}$, at 20 K. *Acta Crystallographica*, C40, 1658–1662.

Becker, P.J., and Coppens, P. (1974) Extinction within the limit of validity of the Darwin transfer equations: I. General formalism for primary and secondary extinction and their application to spherical crystals. *Acta Crystallographica*, A30, 129–147.

Berman, R.G. (1990) Mixing properties of Ca-Mg-Fe-Mn garnets. *American Mineralogist*, 75, 328–344.

Born, L., and Zemann, J. (1964) Abstandsberechnungen und gitterenergetische Berechnungen an Granaten. *Beiträge zur Mineralogie und Petrologie*, 10, 2–23.

Cressey, G. (1981) Entropies and enthalpies of aluminosilicate garnets. *Contributions to Mineralogy and Petrology*, 76, 413–419.

Destro, R. (1988) Experimental determination of scan-truncation losses from low-temperature (16 K) single-crystal X-ray measurements. *Australian Journal of Physics*, 41, 503–510.

Downs, R.T., Gibbs, G.V., Bartelmehs, K.L., and Boisen, M.B., Jr. (1992) Variations of bond lengths and volumes of silicate tetrahedra with temperature. *American Mineralogist*, 77, 751–757.

Geiger, C.A., Newton, R.C., and Kleppa, O.J. (1987) Enthalpy of mixing of synthetic almandine-grossular and almandine-pyrope garnets from high temperature solution calorimetry. *Geochimica et Cosmochimica Acta*, 51, 1755–1763.

Geiger, C.A., Merwin, L., and Sebal, A. (1992) Structural investigation of pyrope garnet using temperature-dependent FTIR and ^{29}Si and ^{27}Al MAS NMR spectroscopy. *American Mineralogist*, 77, 713–717.

Giacovazzo, C. (1992) *Fundamentals of crystallography*, 654 p. Oxford University Press, Oxford, U.K.

Gibbs, G.V., and Smith, J.V. (1965) Refinement of the crystal structure of synthetic pyrope. *American Mineralogist*, 50, 2023–2039.

Haselton, H.T., and Westrum, E.F. (1980) Low temperature heat capacities of synthetic pyrope, grossular and pyrope₆₀grossular₄₀. *Geochimica et Cosmochimica Acta*, 44, 701–709.

Hazen, R.M., and Finger, L.W. (1982) *Comparative crystal chemistry*, 231 p. Wiley, New York.

Hofmeister, A.M., and Chopelas, A. (1991) Thermodynamic properties of pyrope and grossular from vibrational spectroscopy. *American Mineralogist*, 76, 880–891.

Kieffer, S.W. (1979a) Thermodynamics and lattice vibrations of minerals: 1. Mineral heat capacities and their relationships to simple lattice vibrational models. *Reviews of Geophysics and Space Physics*, 17, 1–19.

— (1979b) Thermodynamics and lattice vibrations of minerals: 2. Vibrational characteristics of silicates. *Reviews of Geophysics and Space Physics*, 17, 20–34.

— (1979c) Thermodynamics and lattice vibrations of minerals: 3. Lattice dynamics and an approximation for minerals with application to simple substances and framework silicates. *Reviews of Geophysics and Space Physics*, 17, 35–59.

— (1980) Thermodynamics and lattice vibrations of minerals: 4. Application to chain and sheet silicates and orthosilicates. *Reviews of Geophysics and Space Physics*, 18, 862–886.

Koziol, A.M., and Bohlen, S.R. (1992) Solution properties of almandine-pyrope garnet as determined by phase equilibrium experiments. *American Mineralogist*, 77, 765–773.

Kuhs, W.F. (1988) The anharmonic temperature factor in crystallographic structure analysis. *Australian Journal of Physics*, 41, 369–382.

Meagher, E.P. (1975) The crystal structure of pyrope and grossularite at elevated temperatures. *American Mineralogist*, 60, 218–228.

Novak, G.A., and Gibbs, G.V. (1971) The crystal chemistry of the silicate garnets. *American Mineralogist*, 56, 791–825.

Pilati, T., Demartin, F., and Gramaccioli, C.M. (1993a) Atomic thermal parameters and thermodynamic functions for corundum ($\alpha\text{-Al}_2\text{O}_3$) and bromellite (BeO): A lattice dynamical estimate. *Acta Crystallographica*, A49, 473–480.

Pilati, T., Demartin, F., Cariati, F., Bruni, S., and Gramaccioli, C.M. (1993b) Atomic thermal parameters and thermodynamic functions for chrysoberyl (BeAl_2O_4) from vibrational spectra and transfer of empirical force fields. *Acta Crystallographica*, B49, 216–222.

Robinson, K., Gibbs, G.V., and Ribbe, P.H. (1971) Quadratic elongation: A quantitative measure of distortion in coordination polyhedra. *Science*, 172, 567–570.

Rossmann, E., Kumpat, G., and Schulz, A. (1990) N-beam interactions examined with the help of the computer programs PSIINT and PSILAM. *Journal of Applied Crystallography*, 23, 99–104.

Sawada, H. (1993) The crystal structure of garnets: I. The residual electron density distribution in pyrope. *Zeitschrift für Kristallographie*, 203, 41–48.

- Smith, J.V., Artioli, G., and Kvik, Å. (1986) Low albite, $\text{NaAlSi}_3\text{O}_8$: Neutron diffraction study of crystal structure at 13 K. *American Mineralogist*, 71, 727–733.
- Winkler, B., Dove, M.T., and Leslie, M. (1991) Static lattice energy minimization and lattice dynamics calculations on aluminosilicate minerals. *American Mineralogist*, 76, 313–331.
- Zemann, A., and Zemann, J. (1961) Verfeinerung der Kristallstruktur von synthetischem Pyrop $\text{Mg}_3\text{Al}_2(\text{SiO}_4)_3$. *Acta Crystallographica*, 14, 835–837.
- Zemann, J. (1962) Zur Kristallchemie der Granate. *Beiträge zur Mineralogie und Petrologie*, 8, 180–188.

MANUSCRIPT RECEIVED SEPTEMBER 7, 1994

MANUSCRIPT ACCEPTED FEBRUARY 1, 1995